

Experimental characterization of aviation-fuel cavitation

Patrick F. Dunn,^{a)} Flint O. Thomas, Michael P. Davis, and Irina E. Dorofeeva
*Department of Aerospace and Mechanical Engineering, Institute for Flow Physics and Control,
 University of Notre Dame, Notre Dame, Indiana 46556, USA*

(Received 2 February 2010; accepted 23 August 2010; published online 4 November 2010)

The results of an experimental investigation of the gaseous cavitation of JP-8 aviation fuel in a converging-diverging nozzle are presented. Fuel cavitation is experimentally characterized by high-speed digital imaging, static pressure distributions, and nonintrusive void fraction and bubble velocity measurements. For comparative purposes, experiments were performed using distilled water and dodecane for the same nozzle and nozzle pressure ratios. Dodecane, the largest component of JP-8 by weight, served as its single-component surrogate. For each working fluid, the experiments examined two different flow regimes: an initially single-phase liquid flow in which no cavitation occurred and another that evolved into two-phase cavitating flow. Additional experiments were performed to study the effect of air bubbles injected into either water or JP-8 at the nozzle inlet. For a sufficiently low range of imposed back pressures, gaseous cavitation led to choked flow for each working fluid. The character of the cavitation in the three fluids was different. These differences are highlighted and plausible mechanisms responsible for the observed behavior are discussed. © 2010 American Institute of Physics. [doi:10.1063/1.3490051]

I. INTRODUCTION

This paper presents the results of an experimental investigation into several fundamental aspects of aviation-fuel cavitation. The occurrence of cavitation in an aircraft fuel system can lead to unexpected degradation in system performance and/or damage to fuel system components. This investigation was aimed at gaining a better understanding of some aspects of cavitation behavior in modern aircraft fuel systems. These systems often are characterized by complex internal flow geometries that involve very narrow flow path restrictions and sharp turns. Such geometries can lead to localized regions of high fluid velocity and low static pressure near the liquid vapor pressure.

For some scenarios in which the static pressure is close to but above the liquid vapor pressure, gaseous cavitation occurs. For other scenarios, the static pressure can go below the liquid vapor pressure, leading to both gaseous and vaporous cavitations. In some systems the fuel is utilized to cool avionics, which elevates its vapor pressure and adds to the likelihood that vaporous cavitation will occur. Solid micro-particles in the form of silicates and iron oxides typically are present in aviation fuel. These harbor numerous nucleation sites for cavitation inception. Further, internal flow paths provide a source of wall nucleation sites. The dissolved gas content of the fuel, which is a cumulative effect of its storage and handling history, adds additional complexity.

The working fluid of primary interest for these experiments is JP-8. This aviation fuel is used most commonly by the United States military.¹ JP-8 consists of distillate process streams refined from crude petroleum. It is a complex mixture of over 228 hydrocarbons and additives to meet military specification MIL-DTL-83133.^{2,3} It is comprised of 18% (by

volume) aromatics, 20% naphthenes, 60% paraffins, and 2% olefins.⁴ The main constituent of JP-8 is kerosene, which consists of hydrocarbons, primarily in the C₉ to C₁₆ range.⁵ JP-8 is closely related to Jet A-1. One notable difference is additives in JP-8 that are required for military applications. These include an icing inhibitor (to prevent precipitation of ice crystals at high altitude), a corrosion inhibitor, and a static discharge inhibitor. Details regarding the bulk fluid properties and the chemical composition of JP-8 can be found elsewhere.³

A vast body of literature exists regarding cavitation in water primarily because of marine applications. The interested reader is referred to the monographs by Knapp,⁶ Young,⁷ and Brennen.^{8,9} Various aspects of cavitation have been the focus of comprehensive reviews by Plesset and Prosperetti,¹⁰ Arndt,^{11,12} Blake and Gibson,¹³ and Dowson and Taylor,¹⁴ to name but a few. With the exception of work done on cavitation in fuel injector nozzles for diesel engines (for example, see Refs. 15 and 16), no studies can be found in the open literature involving fundamental aspects of cavitation in hydrocarbon fuels.

No attempt is made here to investigate fuel cavitation as it actually occurs in the full complexity of an aircraft fuel system. Rather, a comparatively simple, generic, flow-field geometry was selected for this experimental investigation: a two-dimensional converging-diverging (C-D) nozzle. Details regarding specifics of the nozzle geometry are presented in Sec. II. Although simple, the C-D nozzle is capable of reproducing several key aspects of fuel cavitation. These include nucleation, bubble growth, and its associated flow compressibility, bubble collapse, and choking. It also is accessible for flow-field diagnostics. Unlike in hydrodynamic cavitation experiments for marine applications where there are typically many orders of magnitude between the length scales of the experimental apparatus and prototype flow, the characteristic

^{a)}Author to whom correspondence should be addressed. Electronic mail: pdunn@nd.edu. Telephone: 001 574 631 6089.

dimensions of the experimental C-D nozzle geometry used in this investigation are comparable to those of aircraft fuel system components. It is known that the total pressure affects the inception and structure of cavitation in internal flows. The total pressure can range from atmospheric pressure at altitude in the fuel tank (where the velocity is near-zero and the pressure is less than the atmospheric pressure at sea level) to several hundreds of psi. Velocities in the pump feed lines are $O(1 \text{ cm/s to } 10 \text{ m/s})$, leading to static pressures comparable to the total pressures there. Higher total pressures occur after the boost and piston pumps, which are located downstream of the fuel tank. Beyond these pumps, the differences between static and total pressures increase significantly. The operating total pressures in aircraft fuel pumps can range from 50 psi ($\sim 340 \text{ kPa}$) (minimum inlet pressure) to as high as 3000 psi ($\sim 20 \text{ MPa}$) (maximum exit pressure). Within the pump, in some situations, static pressures are reduced by flow channel restrictions [$O(1 \text{ mm to } 1 \text{ cm})$] and sharp turns. Thus, although the total pressures at the pump exit may be relatively high, static pressures near vapor pressure can occur before the pump exit, as evidenced by the occurrence of cavitation within the pump. Finally, as described later, C-D channel flow has been used in many previous experimental investigations of bubbly flow with water as the working fluid. This provides a framework by which to interpret and contrast new fuel cavitation experimental results. Several of these studies are described briefly next.

The effective compressibility associated with the flow of gas bubbles in water through a C-D channel was first described by Tangren *et al.*¹⁷ This early study included a comparison between measured static pressure and model predictions. Muir and Eichorn¹⁸ conducted experiments using air bubbles dispersed in water at pressure ratios sufficient for choked flow through a C-D nozzle. Static pressure measurements were made at three locations within the nozzle: in the converging section, at the throat, and in the diverging section. The initial gas-to-total volume fractions (that is, void fractions) of air-to-water ranged from 0.02 to 0.60, yielding corresponding volume fractions at the throat ranging from 0.10 to 0.86. High-speed photography showed the formation of a “shock” in the diverging portion of the nozzle, which the authors noted resembled “a cloud of smoke.” The pressure measurements obtained by Muir and Eichorn¹⁸ often have been used for comparison with numerical results of various cavitation models. In related work, Sandhu and Jameson¹⁹ investigated the flow of a foam (consisting of air and a solution of a surface-active agent in water) through a C-D channel. Inlet, throat, and exit pressure measurements were reported. Bubbly shocks were also observed. The shock position downstream of the throat and the extent of spatial oscillation of the shock front were observed to increase with increasing initial volume fraction. Another experiment conducted by Thang and Davis²⁰ examined air-water bubbly flows in venturi nozzles with an initial void fraction ranging from 20% to 60%. Measurements similar to those cited in the previous experimental studies were reported. Ishii *et al.*²¹ presented pressure measurements for nonchoked flow through a nozzle with an inlet-to-throat area contraction ratio

of 2.7:1 seeded with dilute nitrogen bubbles. Void fractions for such a mild contraction (and, hence, for a small flow acceleration) were low ($\sim 5\%$) throughout the entire nozzle. Their results were compared with a model that included a new equation developed for the motion governing the dispersed bubble phase. Agreement between model and experiment was reported.

Several authors developed models of two-phase C-D channel flow with varying degrees of complexity. Initial attempts neglected bubble dynamics and used a barotropic model that assumed fluid pressure was only a function of fluid density (for example, see Ref. 8). In such models, the only effect of the bubbles is to add an effective compressibility to the fluid. Consequently, the two-phase system is modeled as one compressible phase. A mixture sonic speed, which is a function of void fraction, can be calculated using the barotropic relation. Model inputs are the single-phase fluid properties and the initial void fraction. Outputs include the mixture sonic speed and the critical throat-to-inlet pressure ratio at which the nozzle becomes choked (because of the effective compressibility of the two-phase mixture).

In reality, bubble dynamics are likely to be quite important in two-phase nozzle flows. So, it is not surprising that many authors have sought to incorporate this effect into their models. A steady state model was developed by Wang and Brennen²² that couples a quasi-one-dimensional, inviscid flow model with the Rayleigh–Plesset equation. Stable solutions were obtained only for very small initial void fractions; above an initial void fraction of 3×10^{-6} the solutions became unstable, with the flow “flashing” entirely to vapor and fluid velocities increasing without bound. A perturbation analysis of this instability was reported.²³ This analysis provided critical values of the initial void fraction as a function of several relevant flow parameters. An unsteady model²⁴ demonstrated that the unstable flashing solutions of the Wang and Brennen²² model actually involve unsteady shock waves propagating in the nozzle. Both of these models require specification of the inlet bubble void fraction *a priori*. Delale *et al.*²⁵ considered quasi-one-dimensional cavitating flow in a nozzle. They utilized a modified form of the Rayleigh–Plesset equation that took into account bubble-bubble interactions. In addition, classical damping mechanisms were accounted for via an effective viscosity term. More recently, the range of inlet conditions that yielded stable solutions for the steady model were extended by including a homogeneous nucleation model for cavitation inception in their continuum bubbly flow model.²⁶ Under certain *ad hoc* assumptions, including specific values for a Gibbs activation energy correction factor, a critical bubble radius, and a ratio involving the dissolved gas pressure, vapor pressure, and static pressure, the model was capable of predicting a steady “bubbly shock wave” in the diverging section of the nozzle.

Differences between cavitating flows of water and JP-8 are anticipated not only because of differences in bulk fluid properties (density, surface tension, and viscosity), but also because JP-8 is a complex multicomponent mixture. Each component has a slightly different surface tension and a different vapor pressure. For example, the difference in vapor pressure between the most and least volatile components of

JP-8 spans three orders of magnitude. The presence of multiple components in a fluid thereby admits the possibility of cavitation bubbles of different sizes forming and collapsing at different local static pressures within the nozzle. It also complicates the cavitation inception scenario because nascent bubbles forming from one component at a given vapor pressure could serve as nuclei for a component with a slightly lower vapor pressure. Further, the average vapor pressure appears to be a function of both mixture variability and storage history.²⁷ Microparticles are usually present within the fuel. It has been shown in numerous studies^{28–31} that these microparticles harbor nucleation sites, making it more complex to determine where and under what flow conditions cavitation will first occur.

The primary objectives of the experimental investigation reported in this paper are as follows.

- (1) To provide measurements characterizing aviation-fuel cavitation in a C-D nozzle, focusing almost exclusively on gaseous cavitation. These measurements are performed in a relatively simple geometry, which is, nonetheless, capable of producing some essential features of fuel cavitation, including nucleation, effective compressibility effects including choking, and bubble collapse. Experimental diagnostics include high-speed imaging, channel static pressure distributions of high spatial resolution, void fraction distributions, and bubble velocity measurements.
- (2) To compare and contrast the character of gaseous cavitation occurring in JP-8 fuel and in distilled water under identical channel geometry and flow conditions. Additionally, comparisons are made with dodecane. The experiments using dodecane represent those of a single-component surrogate for JP-8 with a well-defined vapor pressure.

The remainder of this paper is organized as follows: the experimental facility and diagnostics are described in detail in the next section. This is followed by presentation of experimental results for JP-8, distilled water, and dodecane. Additional measurements involving controlled bubble injection into water and JP-8 at the nozzle inlet and its effects on pressure, void fraction, bubble velocity, and shock location are presented. Finally, implications of the experimental results are given in the discussion and conclusions section.

II. DIAGNOSTICS

The two-dimensional C-D nozzle used in this study was part of a dedicated flow facility. High-pressure internal flow systems require large mass flow rates to reach static pressures sufficiently low to achieve cavitation. Because using large amounts of fuel was prohibitive and posed safety issues, the facility was designed to accommodate manageable fuel flow rates (~ 3.8 L/min or ~ 1 gal/min). Cavitation was achieved in the test section at these relatively lower mass flow rates by biasing the facility reference pressure in a blow-down configuration. The test section was large enough for the required diagnostics and comparable in

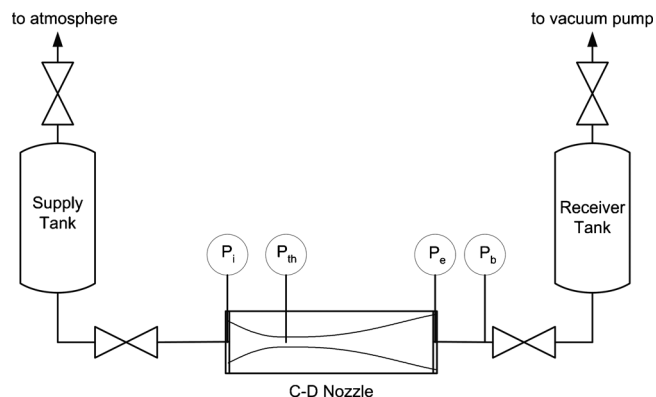


FIG. 1. Schematic of the C-D nozzle cavitation facility (components not to scale).

flow cross-sectional area to that found in aircraft fuel system components.

A. Experimental facility and procedure

A schematic of the experimental facility is shown in Fig. 1. Two stainless steel, 38 L tanks were the liquid reservoirs. Initially, the upstream tank was filled with the working fluid and was open to atmospheric pressure. The downstream tank was isolated from the system with a valve and evacuated by a vacuum pump (Dekker model RVL020W-01) to the desired back pressure, P_b . The back pressure was measured using a vacuum pressure gage (Dwyer series SGL 4.5 in., 0 kPa to -100 kPa absolute, 1% accuracy). The pressure differential between the upstream and downstream tanks drove the flow. Flow was initiated when the valves between the two tanks were opened and the upstream tank emptied through the C-D nozzle into the downstream tank. The volumetric flow rate of the liquid was measured using a magna-helix flow meter placed upstream of the nozzle test section (Dwyer series RMV Rate-Master, 0 gal/min to 5 gal/min, 2% of full-scale accuracy). For those experiments in which air was injected into the nozzle inlet (to control the initial void fraction), the air flow rate was measured using a primary-standard airflow-measurement system (Sensidyne Gilian Gilibrator2 Calibration System, 1 cm^3/min accuracy).

A schematic of the nozzle geometry is shown in Fig. 2. Only two walls of the C-D nozzle were contoured. The other two sidewalls were flat. This resulted in a channel with a rectangular cross-section. The nozzle contour was machined out of a rectangular piece of Plexiglas[®] to a depth of 1.6 mm. A flat cover plate sealed the nozzle using a rubber O-ring. The nozzle-wall contour was designed using a fifth-order polynomial fit to ensure zero-slope conditions at the inlet, exit, and throat transitions. The length of the diverging

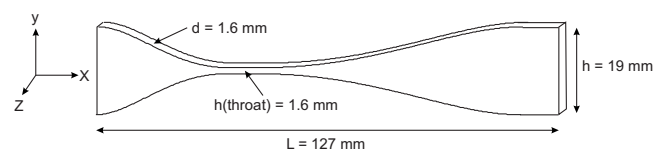


FIG. 2. Schematic of the C-D nozzle.

section was chosen so that the maximum slope of each wall never exceeded 7° to prevent flow separation. The overall length of the nozzle, L , was 127 mm. The nozzle throat area was constant from $x=24.1$ mm to $x=33.5$ mm. This corresponded to x/L values from 0.19 to 0.26. The inlet and exit heights, h , were both 19 mm, and the throat height was 1.6 mm. This gave a nozzle inlet-to-throat area ratio of 12:1 ($30 \text{ mm}^2:2.5 \text{ mm}^2$).

B. Fluid characterization

Three fluids were used in this investigation: aviation fuel (JP-8), dodecane [$\text{CH}_3(\text{CH}_2)_{10}\text{CH}_3$, which is denoted more conveniently as $\text{C}_{12}\text{H}_{26}$], and distilled/de-ionized water. JP-8 was the fluid of primary interest. Dodecane is the largest constituent of JP-8 by percent weight (22.54%) and served as the single-component fluid (with a well-defined vapor pressure) representative of JP-8. Water was used mainly to validate the experimental technique and serve as a basis for comparison with fuel cavitation under the same nozzle operating conditions.

The property values of JP-8 can differ because of variability in its mixture, as well as its storage history and location. For example, the vapor pressure of JP-8 gathered from seven different locations in the U.S. ranged from 74 Pa to 430 Pa (at 294 K), with an average vapor pressure of 240 Pa.²⁷ The average vapor pressure, based on the percent weight of the first 12 components that comprise greater than 99% of the weight of JP-8, is 575 Pa. The highest component vapor pressure is 6500 Pa (isooctane, 3.66 wt %). The lowest component vapor pressure is 8 Pa (1-methylnaphthalene, 3.49 wt %). So, for JP-8, the vapor pressures among its constituents range from 8 Pa to 6500 Pa, and, for itself, from approximately 74 Pa to 430 Pa. Dodecane's vapor pressure is 16 Pa (at 298 K).³² The vapor pressure of distilled water is 2123 Pa (at 294 K).³³ The densities of the liquids at 298 K were 997 kg/m^3 for water, 796 kg/m^3 for JP-8, and 752 kg/m^3 for dodecane. The surface tensions at 298 K were 0.072 N/m for water, 0.023 N/m for JP-8, and 0.025 N/m for dodecane.

One objective of this study was to examine the cavitation behavior of JP-8 stored under typical conditions without any special treatment or handling. The JP-8 used in these experiments was stored at ambient temperature and pressure ($\sim 294 \text{ K}$ and $\sim 101.3 \text{ kPa}$, respectively) in closed, 3.8 L containers until an experiment was performed. Under these ambient conditions, the dissolved content of air in JP-8 is $0.139 \text{ mm}^3 \text{ air/mm}^3 \text{ fuel}$ (based on 78% of N_2 and 21% O_2 , having solubilities of $0.120 \text{ mm}^3 \text{ N}_2/\text{mm}^3 \text{ fuel}$ and $0.215 \text{ mm}^3 \text{ O}_2/\text{mm}^3 \text{ fuel}$, respectively).³ The fuel was obtained commercially and was not degassed prior to experiment. Subsidiary experiments were conducted in which pressure measurements within the C-D nozzle were made immediately after filling the nozzle supply reservoir, after 24 h, and after 48 h. A comparison of the resulting pressure distributions showed that the static pressures varied by less than 2% at each location between these experiments. This variation was within the experimental uncertainty of the

pressure measurement. In almost all cases reported herein, experiments were conducted within 4 h after filling the reservoir.

C. Surface characterization and microparticle effects

JP-8 in its natural, unsettled state contains solid microparticles in the form of iron oxides and silicates. Data provided by the Honeywell Corporation indicated a particle mass concentration of $\sim 2 \text{ mg/L}$ fuel and a number concentration of $\sim 10^7$ particles/l fuel. Microscopic pits on the surface of microparticles can serve as bubble nucleation sites. The diameters of microbubbles statically resident on these sites when submerged in JP-8 were characterized by microscopic examination. Two site characteristics were obtained: the size distribution of nucleation sites and their area density (number of sites per unit particle surface area). The measured size distribution was approximately log-normal with a mean diameter of $10.7 \mu\text{m}$, and had approximately 70% of the nucleation sites less than $10 \mu\text{m}$ in diameter and approximately 90% less than $20 \mu\text{m}$. The site area density was $3600 \pm 500 \text{ sites/mm}^2$. These characteristics imply that there are approximately 10^6 microparticle nucleation sites/l of unsettled or unfiltered JP-8.

The internal surface of the C-D nozzle test section was Plexiglas[®]. Its surface in the region of initial bubble formation was examined microscopically with submersion of the surface in either JP-8 or distilled water. For both liquid cases, all nucleation site diameters were less than $30 \mu\text{m}$. The mean diameter for JP-8 was $8.2 \mu\text{m}$, with 70% of the pit diameters being less than $10 \mu\text{m}$. That for water was $10.5 \mu\text{m}$, with 34% of diameters being less than $10 \mu\text{m}$. Both distributions were approximately log-normal. The nucleation site area densities found were 220 sites/mm^2 for JP-8 and 300 sites/mm^2 for water. The measurement uncertainties at the 95% confidence level were $\pm 1 \mu\text{m}$ for the diameter and $\pm 0.5\%$ for the site area density. The nozzle-wall site area densities were approximately an order of magnitude less than that for the microparticles themselves. The mean diameters of the sites for all wetted surfaces, however, were approximately the same ($\sim 10 \mu\text{m}$).

Each of the liquids used in the present experiments was essentially free of particles. The distilled/de-ionized water was obtained from a filtered laboratory water-purification system. The dodecane was purchased commercially in 5 L containers. While the JP-8 did contain microparticles, as described previously, these were effectively filtered from the JP-8 over time by gravitational settling in the storage tanks. The JP-8 for an experiment then was drawn from the top of the storage tanks to fill the facility's supply tank. Hence, for the experiments reported in this study, nucleation sites for gaseous cavitation resided primarily on the channel walls.

Subsidiary experiments were conducted with microparticles mixed in the fluid to examine their effect on the location of cavitation inception and the structure of the resulting flow. Microparticles filtered from JP-8 were added to distilled water in various concentrations. With no microparticles present, cavitation was observed to originate from the nozzle walls. With microparticles present in sufficient quantities,

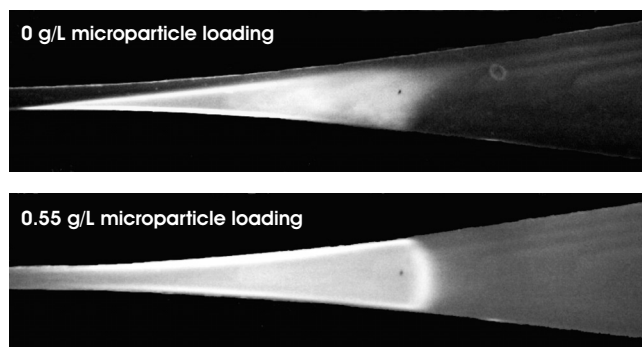


FIG. 3. Digital images of distilled water without microparticles (top) and with microparticles (bottom) at 0.55 g/l loading showing cavitating C-D nozzle flow over the divergent section from $x/L \approx 0.3$ to $x/L \approx 0.7$. Flow is from left to right. The frame rate is 30 frames/s.

cavitation initiated within the bulk of the fluid. Figure 3 shows two images from the same viewing perspective of the cavitating flow of water at the same flow rates and pressures. In the top image, the fluid does not contain microparticles. Cavitation initiates at the lower wall of the nozzle throat. The streamwise locations of bubble collapse in the diverging section of the nozzle varied in the cross-stream direction. In the bottom image, the fluid contains filtered microparticles with a concentration of 0.4 g/L. Cavitation initiates again in the nozzle throat but now within the bulk fluid (also, possibly from the walls) and across the entire nozzle throat cross-stream direction. The location of the bubble collapse occurs at approximately the same x/L location as in the previous image, but is more uniform in the cross-stream direction.

Microparticles present in the fluid at this concentration cause the bulk of cavitation initiation to occur on particle surfaces (as opposed to wall surfaces) and spatially organize the cavitating flow and bubble-collapse region. Indeed, void fraction measurements (their method to be described later) acquired for different microparticle concentrations (from 0 g/L to 0.55 g/L) confirm a more distinct region of bubble collapse when microparticles are present. However, it is important to note that particle loading concentrations approximately 100 times greater than those typical of JP-8 samples (>200 mg/L) were required to achieve any measurable difference in void fraction. This being the case, the gravitational filtering of JP-8 effectively eliminated microparticles as nucleation sources in the reported experiments.

D. Repeatability of results

The main factors that govern onset and structure of the cavitating flow were controlled either directly or indirectly. This was done to the extent that *all of the experimental measurements were repeatable to within their reported uncertainty at the 95% confidence level*. The experimental results were obtained over a period of 3 years by two different investigators using at least four different C-D nozzles of similar material and many samples of each liquid taken from different sources. The aviation fuel, for example, was obtained twice from the Honeywell Corporation and twice from a local airport, all at different times over this period. The distilled/de-ionized water was drawn numerous times during

this period from the filtered water-purification system. The dodecane was purchased commercially from different vendors several times.

E. Pressure measurements

The axial static pressure distribution in the nozzle was measured using an array of pressure transducers (Setra model 209). The transducer response time was 5 ms. Static pressure taps, 0.33 mm in diameter, were drilled normal to the test section cover plate along the centerline of the nozzle and were connected to the transducers using plastic tubing. Care was taken to ensure that this linear array of wall static pressure taps was hydrodynamically smooth. The taps were spaced at intervals of 3.2 mm over the 12.7 cm length of the nozzle, resulting in 40 measurement locations. The pressures were acquired via a PC running LABVIEW[®] over a sampling period of ~ 30 s at a sampling frequency of 20 kHz. The receiver tank back pressure and all pressure measurements remained constant over the duration of the data acquisition. Pressure measurements were made at several different imposed back pressures (hence, different nozzle exit pressures) for all the liquids. Typically, a distilled water case was repeated at least ten times, and a fuel or dodecane case at least two or three times. The relative uncertainty of the measured mean static pressures was 3% (estimated at the 95% confidence level). Pressures reported herein are fully converged temporal averages.

Some experiments were conducted to examine the effect of back pressure on the nozzle flow rate for all three fluids. These experiments identified the range of back pressures over which the mass flow rate through the nozzle was choked.

As used here, the term choked implies that the nozzle mass flow rate became invariant with further reduction in imposed back pressure (or nozzle pressure ratio), which is indicative of sonic conditions at the throat. It is worth noting that choking in a cavitating venturi has been used as a means to control the liquid fuel and oxidizer flow rates in rocket engines despite pressure fluctuations.³⁴

Sample results are presented for water in Fig. 4. Similar behavior was seen for dodecane and JP-8. As the back pressure was reduced from 100 kPa, the mass flow rate increased until the back pressure reached a critical value. Starting at this pressure, the flow rate remained constant as the back pressure was decreased further, which established that flow in the nozzle was choked. The critical back pressures for choking, P^* , were approximately 56 kPa, 54 kPa, and 50 kPa for distilled water, dodecane, and JP-8, respectively. This corresponded to critical pressure-to-inlet pressure ratios, P^*/P_o , of 0.55, 0.53, and 0.49, respectively.

F. High-speed digital imaging/void fraction

High-speed digital imaging was used to visualize the instantaneous structure of the two-phase nozzle flow and to determine the local void fraction and bubble velocity. A FASTCAM-ultima APX model high-speed video acquisition system (PHOTRON Limited) was used to capture the high-speed images. The system was capable of frame rates from

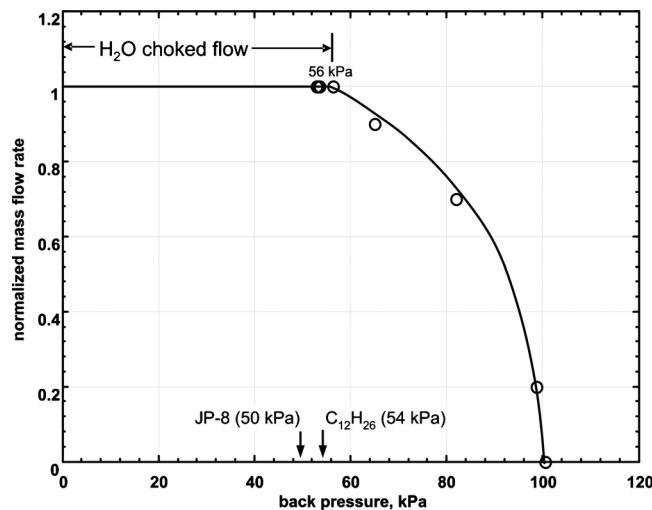


FIG. 4. Normalized mass flow rate as a function of receiver tank back pressure for H₂O. Also indicated by arrows for both dodecane and JP-8 are the upper limits of the back pressure regions over which flow was choked.

2000 frames/s at full resolution (1024 pixels by 1024 pixels) to 120 000 frames/s at reduced resolution (128 pixels by 16 pixels). The exposure duration could be set independently of frame rate to any value from that of the inverse of the frame rate to as short as 4 μ s/frame. Typical camera settings used while photographing the cavitating flow had a resolution of 1024 pixels by 256 pixels, a frame rate of 8000 frames/s (the maximum possible for this resolution), and an exposure duration of 8 μ s/frame. At these settings, the duration of an acquired video record was slightly over 1 s. Because the flow transit times through the C-D nozzle were on the order of 10 ms, the exposure durations were approximately 1/1000 of the flow transit time. This essentially gave “instantaneous” images of the flow. In the extreme case (the smallest bubble traveling at the highest velocity), some blurring of bubbles in the image did occur (mainly when using JP-8). For this situation, a bubble would travel approximately one bubble diameter during an exposure. The frame rate used yielded approximately 800 entire flow transits over the nozzle length for each experimental condition. This assured that a thorough visual history of the flow was obtained.

G. Void fraction measurements

The distribution of the liquid-gas void fraction along the length of the nozzle was determined from a record of successive high-speed digital images. Advantages of this approach were that it was noninvasive, compatible with all fluids of interest, and able to distinguish clearly between gas and liquid phases. Further, the effective frequency response of this approach was greater than 10 MHz. Other invasive techniques (using either resistivity or hot-film probes) were attempted and were less successful, especially for the smaller bubbles encountered in the JP-8 experiments.³⁵

The void fraction, α , for a liquid-gas mixture is defined as

$$\alpha \equiv V_g / (V_g + V_l), \quad (1)$$

where V_g is the gas volume and V_l is the liquid volume. Time- and space-averaged pixel intensities of images of the x, y directional plane of the flow (see Fig. 2) and their projection into the z direction (depth) of the flow were used to determine the local gas and liquid volumes, and, thus, the void fraction. The contrast between the gas and liquid phases was increased by backlighting the flow within the nozzle with a diffuse light source. Dark regions corresponded to the gas phase; light regions to the liquid phase. An example image that illustrates the results of phase contrasting is presented at the top of Fig. 5.

Image analysis to determine the void fraction proceeded first by calculating the time-averaged pixel intensity at a particular x, y location within a square interrogation region of 3 pixels by 3 pixels ($\Delta x = 13.7 \mu\text{m}$ by $\Delta y = 13.7 \mu\text{m}$). The dimensions of the interrogation region were chosen to be smaller than the smallest bubble observed in any of the experiments. This assured, in almost all instances, that either gas or liquid completely occupied the interrogation region.

The spatial average intensity of all nine pixels within the interrogation region at a particular time, $I(t, x, y)$, was determined. A threshold filter was applied to compensate the rare instances when all 9 pixels did not have the same intensity, such as when the edge of a gas void was in the interrogation region. This approach resulted in the phase scalar, $X(x, y, t)$, determined by the conditions

$$X(x, y, t) = \begin{cases} 1 & \text{if } I(x, y, t) > P \\ 0 & \text{if } I(x, y, t) < P, \end{cases} \quad (2)$$

where P is a threshold pixel intensity used to distinguish between the two phases. Thus, for a given time and x, y location, the phase was considered to be either gas [$X(x, y, t) = 1$] or liquid [$X(x, y, t) = 0$] within the interrogation region. The conditional scheme was not overly sensitive to the value of the threshold. Typically, a value of P was set within the range from 30 to 65 (for water) or from 40 to 55 (for fuel), based on an inverted, 0-to-100 normalized pixel intensity scale (“0” pixel intensity value is white; “1” pixel intensity value is black).

Two sequential, magnified images of a region of the flow are shown at the bottom of Fig. 5. For the left image, a “dark” gas void covers the interrogation region contained within the white-bordered box. $I(x, y, t)$ is greater than P and, thus, $X(x, y, t) = 1$. For the right image, which is the next image in the sequence, the gas void has convected downstream and the liquid occupies the interrogation region outlined by the white-bordered box. $I(x, y, t)$ is less than P and, thus, $X(x, y, t) = 0$.

The phase scalar $X(x, y, t)$ was averaged over time to yield the time-mean phase scalar, $\bar{X}(x, y)$, given by the expression

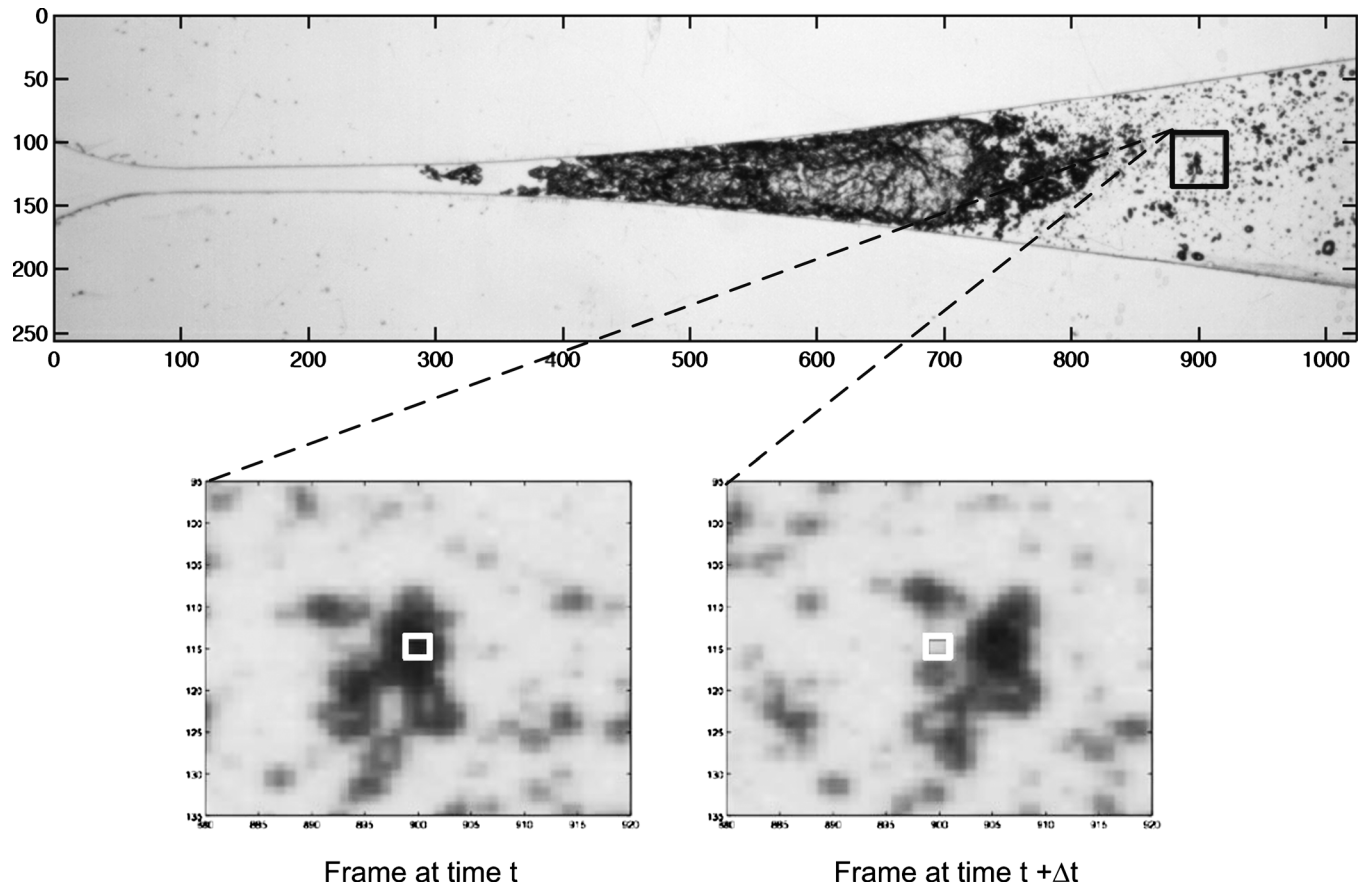


FIG. 5. Top: 1024 pixel (x direction) by 256 pixel (y direction) digital image of cavitating water in the nozzle from $x/L \approx 0.1$ to $x/L \approx 1.0$. Flow is from left to right. Bubbles appear as dark structures; the liquid phase as bright regions. Bottom: two sequential magnified images of the black-bordered region of the flow in which the interrogation region, centered at the pixel coordinates (900,115), is indicated by the white-bordered region. The frame rate was 8000 frames/s with an exposure duration of $6.7 \mu\text{s}$.

$$\bar{X}(x,y) = \frac{1}{T} \int_0^T X(x,y,t) dt, \quad (3)$$

$$\bar{X}(z) = \frac{1}{d} \int_0^d X(z) dz, \quad (6)$$

where T was the total time record length of a sequence of images. T was chosen to be long enough to achieve a sufficiently converged value of $\bar{X}(x,y)$. Convergence was obtained to within 10% of the final value by ~ 500 frames, which corresponded to $T \approx 34$ ms.

The time-mean phase scalar was subsequently integrated in the y (cross-stream) direction over the local height of the nozzle, $h(x)$, to yield the mean phase scalar at that x location, $\bar{X}(x)$, defined as

$$\bar{X}(x) = \frac{1}{h(x)} \int_0^{h(x)} \bar{X}(x,y) dy. \quad (4)$$

This phase scalar represents the spatial-temporal average of the ratio of area of the gas to the total area, where the total area equals $\Delta x h(x)$.

Finally, the void fraction at a given x location was determined as

$$\alpha(x) = [\bar{X}(x)] \cdot [\bar{X}(z)]. \quad (5)$$

In this expression,

where $\bar{X}(z)$ is the mean phase scalar for the z -direction (nozzle depth) and d denotes the constant nozzle depth.

Digital images were not acquired for the y,z plane because of the very limited access ($d=1.6$ mm). Thus, $\bar{X}(z)$ was estimated based on observations. For almost all cases when gas-liquid flow was present in the nozzle, the gas appeared as *one* void within the z direction. The average depth of a void was observed to be approximately two-third of the nozzle depth, or ~ 1 mm. Thus, the value of $\bar{X}(z)$ was based on the projection of a spherical bubble, centered in the z -direction of the nozzle, with a diameter equal to that of the mean z extent of the observed voids. For these experiments, this approach yielded $\bar{X}(z)=0.32$ and was, to good approximation, independent of the fluid used in the experiment.

The overall uncertainty in the void fraction was estimated not to exceed 10% (at the 95% confidence level) for all experiments in which distinct bubbles occurred. For the case of distilled water, where bubbles coalesced into larger gaseous voids, the maximum uncertainty in void fraction was 15% immediately upstream of the bubbly shock location.

TABLE I. Operating conditions for initially single-phase liquid experiments.

Case	Fluid	P_b (kPa)	Re_{inlet}	Q (L/min)	U_{throat} (m/s)	k_{throat}
1	H ₂ O	60 ± 1	3063	1.9 ± 0.4	12.7	0.563
2	H ₂ O	40 ± 1	5480	3.4 ± 0.4	22.7	0.054
3	H ₂ O	20 ± 1	6125	3.8 ± 0.4	25.3	0.029
4	H ₂ O	15 ± 1	6125	3.8 ± 0.4	25.3	0.025
5	JP-8	60 ± 1	1858	2.3 ± 0.4	15.3	0.490
6	JP-8	40 ± 1	3057	3.8 ± 0.4	25.3	0.043
7	JP-8	20 ± 1	3400	4.2 ± 0.4	28.0	0.027 ^a
8	JP-8	15 ± 1	3400	4.2 ± 0.4	28.0	0.007; ^b 0.028 ^c
9	C ₁₂ H ₂₆	20 ± 1	7500	4.4 ± 0.4	29.3	0.0395

^aAt the average vapor pressure.^bFor the most volatile component.^cFor the least volatile component.

The uncertainty in the bubble velocity as estimated from high-speed digital photography was 1 m/s regardless of the fluid used for the experiment.

III. EXPERIMENTAL RESULTS

Experimental results obtained for the three different liquids are presented in this section. These include high-speed digital images, streamwise distributions of static pressure, and void fraction measurements. In each case, results for water are considered first because they provide a basis for comparison with the JP-8 and dodecane results. By varying the imposed nozzle back pressure, two different flow regimes were examined: a single-phase liquid flow in which no cavitation occurred and another that evolved into two-phase cavitating flow. These are followed by a presentation of results from experiments involving cavitating gas-liquid nozzle flow in which the initial void fraction was controlled systematically by injecting microbubbles of air into the nozzle inlet.

A. Initially single-phase flow experiments

1. Operating conditions

Table I summarizes the different operating conditions for the initially single-phase experiments. For all experiments, the upstream supply-tank pressure was atmospheric. The downstream receiver tank was evacuated to obtain the back pressure values that are shown in the table. The back pressure, P_b , was always less than the nozzle exit pressure, P_e , because of the pressure difference between the C-D nozzle exit plane and the receiver tank (see Fig. 1). For all cases when $P_b \geq 40$ kPa (cases 1, 2, 5, and 6), the flow regime was single-phase liquid throughout the nozzle. For all cavitating flows (cases 3, 4, and 7–9), the flow through the nozzle was choked, as indicated by a constant nozzle mass flow rate that was independent of the back pressure variation. Similarly, for these cases, the throat velocity and throat pressure (presented later) also were found to be independent of nozzle back pressure variation.

The nozzle inlet Reynolds number, Re_{inlet} , for each case (based upon inlet velocity and hydraulic diameter) is shown in Table I. The tabulated Reynolds number values suggest

that the nozzle flow was either transitional or turbulent in each case. Also listed is the cavitation inception index at the throat, k_{throat} , for the cases involving choked flow. This was defined as $2(P_{throat} - P_v)/\rho_l U_{throat}^2$, where P_v is the vapor pressure, ρ_l is the liquid density, and U_{throat} is the liquid speed at the throat.

2. Flow visualization results

An image of the flow (one frame from a high-speed video) through the nozzle is displayed in Fig. 6(a) for the case of water at $P_b = 20$ kPa (case 3 in Table I). The image captures the nozzle flow from $x/L \approx 0.2$ to $x/L \approx 0.8$. As the flow accelerated toward the beginning of the throat (located at $x/L = 0.19$), the pressure was reduced until bubbles began to form near $x/L \approx 0.25$. These initially spherical bubbles grew rapidly downstream of the throat to distort and merge to form relatively large sluglike gas voids. At an axial location of $x/L \approx 0.6$, there was a very abrupt change in the two-phase flow structure. The large gas voids collapsed over a small streamwise region ($\Delta x/L \approx 0.02$) and the bubble content of the liquid was greatly reduced. This bubble-collapse region exhibited many of the characteristics of a stationary shock wave in compressible gas flow. Downstream of the bubble-collapse region, the flow appeared as a dilute mixture of spherical bubbles in the liquid. Near the wall, some bubbles were observed to move upstream toward the bubble-collapse region, indicating local flow reversal and the possibility of shock-induced separation.

The bubble-collapse region shown in Fig. 6(a) is highlighted by presenting an enlarged view ($3\times$) in Fig. 7. This more clearly illustrates the shocklike bubble-collapse region in water. Immediately upstream of the region, the gas content in the flow was high, appearing as a complex-surface gas slug, with no spherical bubbles present. As this gas slug encountered the large pressure increase that occurred in this region (to be discussed), smaller slugs and bubbles were expelled and underwent collapse such that there was a very large reduction in gas content over a very short streamwise length (~ 2.5 mm). It is important to note that this figure is one “instantaneous” ($8 \mu\text{s}$ duration) image of the flow structure. The image suggests that some flow stratification may be present. However, other images in the same sequence show slightly different flow structures. In the mean (over 1 s of acquisition time), mostly well-mixed regions of gas and liquid were observed. Indeed, choked flow occurred within the nozzle for this case. This could not occur if the phases were stratified in the mean.

Figure 6(b) shows one frame depicting the cavitation of JP-8 fuel in the nozzle. As was the case for the water image shown in Fig. 6(a), this image was obtained at $P_b = 20$ kPa (case 7 in Table I). Unlike water cavitation, the bubbles that formed in the JP-8 did not appear to coalesce; they remained as comparatively small, individual, spherical bubbles. Another obvious difference between this case and that of water was the lack of a visually apparent localized bubble-collapse region. The initial bubble growth phase in JP-8 was followed by an almost homogeneous bubbly flow exhibiting much smaller bubbles than in water. Observed bubble diameters in

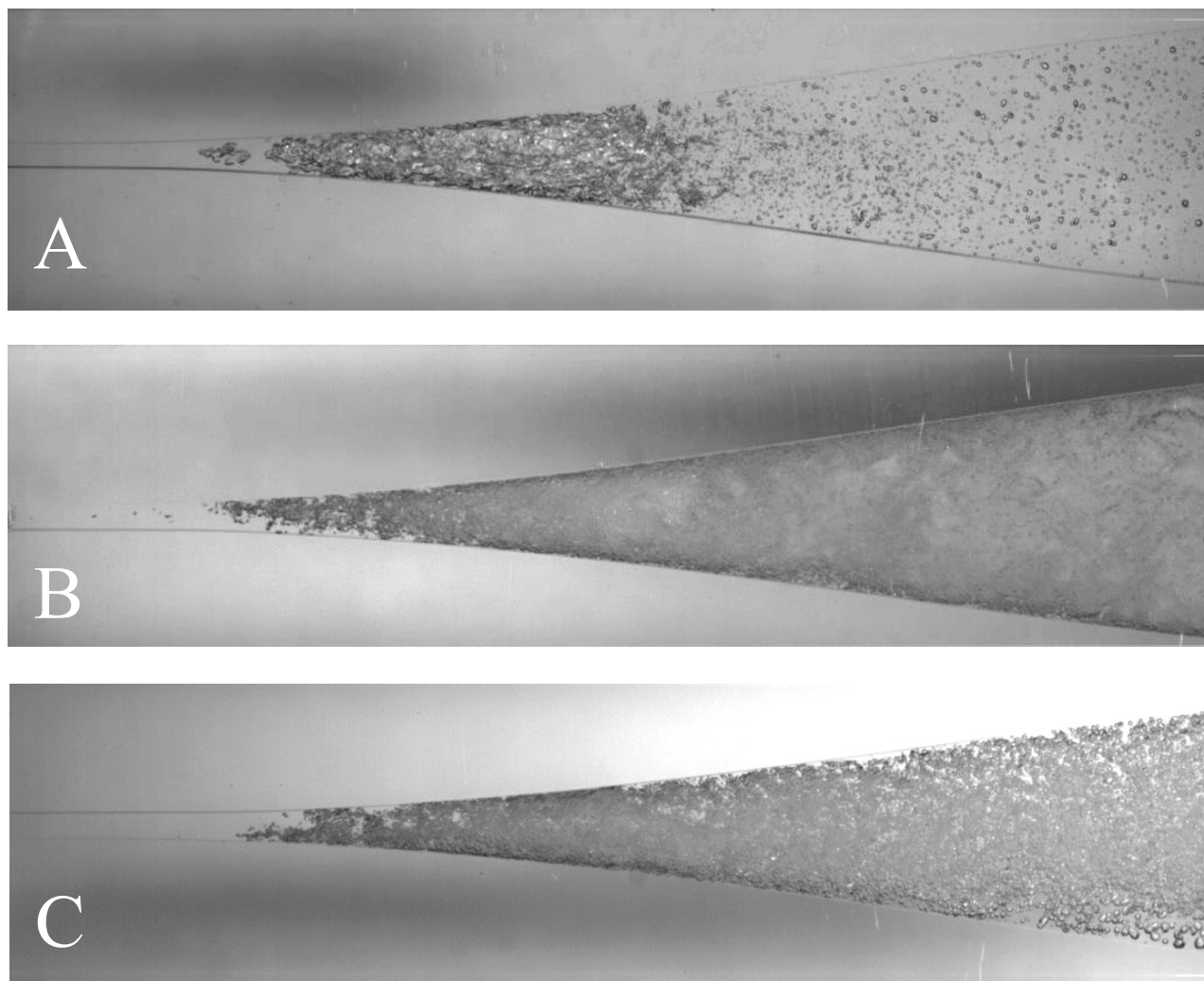


FIG. 6. Images of (a) H₂O, (b) JP-8, and (c) dodecane cavitating mixtures, cases 3, 7, and 9, respectively (frame rate of 15 000 frames/s; exposure duration of 8 μ s) from $x/L \approx 0.2$ to $x/L \approx 0.8$. Flow is from left to right.

JP-8 were approximately 100 μ m, as compared to bubbles typically larger than 1 mm in water. Bubbles remained in the fuel throughout the diffuser section of the nozzle and did not disappear before exiting the nozzle.

An image for the case of dodecane for the same operating conditions as for the JP-8 fuel and water images is presented in Fig. 6(c) (case 9 in Table I). The image is very similar to that of the JP-8 case, but with some subtle differ-

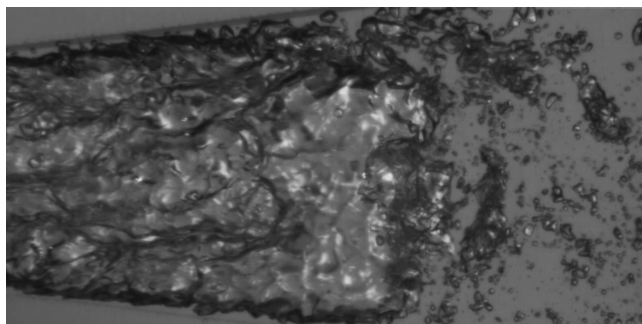


FIG. 7. Close-up of bubble collapse in water, case 3 (frame rate of 15 000 frames/s; exposure duration of 8 μ s) from $x/L \approx 0.4$ to $x/L \approx 0.5$.

ences. On first inspection, no visually obvious bubble-collapse region was apparent. However, the bubbles that persisted in the diverging section of the nozzle appeared much larger than for the JP-8 case.

For each fluid, when cavitation occurred, the local time-mean static pressure was near but above the liquid vapor pressure. As indicated in Table I, the cavitation inception index at the throat (near the location of minimum static pressure) was small but always positive. This supports that the type of cavitation observed in the experiments was gaseous. Further, cavitation is initiated from microscopic gas voids trapped in microscale defects in the C-D channel walls. Because of the nature of the tool path used in machining the nozzle, the number density of nucleation sites was highest near the corners of the channel. High-speed imaging of cavitation inception clearly showed that bubbles originated in the throat near the corners of the C-D channel. It is conjectured that an additional reduction in static pressure associated with streamwise vortices resulting from secondary flow at the channel corners could also play a role in this process, although this aspect was not explored. Cavitation inception at the corners of the channel throat is clearly illustrated in

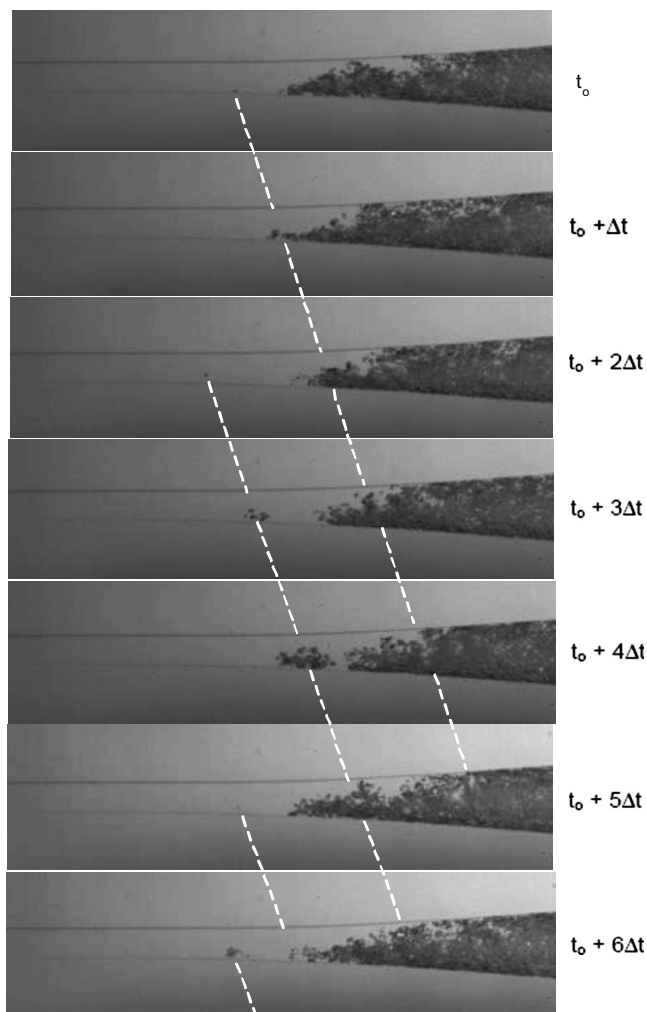


FIG. 8. High-speed images of cavitation inception in dodecane. $\Delta t = 0.125$ ms.

Fig. 8 for the case of dodecane, which has the lowest volatility of any of the fluids examined in this study ($P_v = 21$ Pa). This pressure is two orders of magnitude less than that of water. As indicated by the dashed time-lines in the figure, once the microbubbles departed from the surface, they grew rapidly to fill the channel while convecting downstream. Cavitation occurring at the corners of the nozzle was a consequence the nozzle's two-dimensional geometry and the fluid's negligible level of microparticles.

3. Pressure measurements

In this section, streamwise static pressure distributions obtained along the nozzle centerline are presented. The pressure measurements are normalized by the inlet pressure, P_o , and plotted versus the normalized streamwise spatial coordinate, x/L . In each figure, the nozzle geometry is superimposed on the figure for reference.

The pressures measured for the water case are shown in Fig. 9 (cases 1–4 in Table I). The pressure distributions for cases 1 and 2 are for back pressures that yielded unchoked flow throughout the nozzle. As shown previously in Fig. 4, depending on the imposed back pressure, the effective compressibility associated with cavitation can give rise to chok-

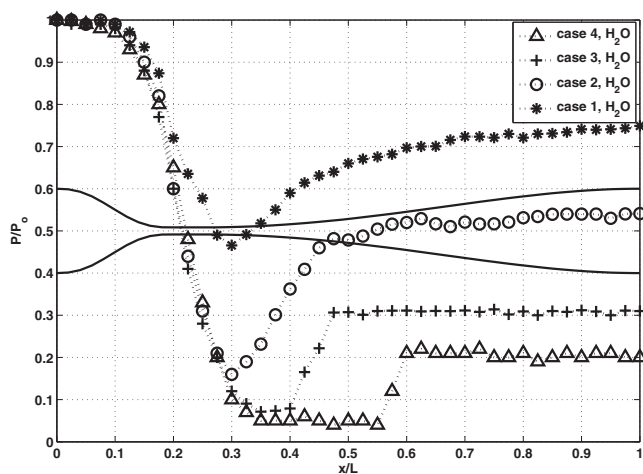


FIG. 9. Axial pressure distribution in H_2O , cases 1–4.

ing of the C-D nozzle. Cases 3 and 4 shown in Fig. 9 correspond to choked flow conditions. Note that in both choked flow cases, the static pressure continued to decrease similarly into the diverging portion of the nozzle. Then, a sudden pressure rise occurred at a different location for each case. The location of this pressure rise corresponded to that of a standing bubbly shock, as seen in previous images in which a distinct region of bubble collapse occurred. Specifically, the shock behavior manifested itself as a relatively sharp increase in pressure beginning at $x/L = 0.40$ and $x/L = 0.55$ for cases 3 and 4, respectively. Beyond these bubble-collapse regions, the pressures remained relatively constant despite the increase in nozzle cross-sectional area. This behavior is indicative of shock-induced flow separation. Contrast this with the attached single-phase flow of cases 1 and 2 where the flow remained attached, with a consequent gradual pressure recovery in the diverging portion of the nozzle. Figure 9 clearly shows that the bubbly shock location was farther upstream (toward the throat) as the back pressure was increased; this is a behavior consistent with compressible gas flow. However, note that the magnitude of the pressure rise across the shock *decreased* with a reduction in back pressure. This is contrary to that for compressible gas flow.

The pressure measurements for JP-8 are presented in Fig. 10 (cases 5–8 in Table I). The profiles for cases 5 and 6 are for unchoked flow. Cases 7 and 8 are for the fully cavitating flow regime, where the pressures from $x/L = 0$ to $x/L \approx 0.35$ were nearly identical in spite of the differences in back pressure. This, in conjunction with the flow rate information presented in Fig. 4, indicated that the flow through the nozzle was choked for these cavitating cases. However, there was no shocklike increase in pressure in the diverging section of the nozzle, as was measured for water. This was consistent with the high-speed imaging of the JP-8 flow that did not display visual evidence of a bubbly shock. Figure 10 shows that the pressure increased comparatively gradually from a minimum value of $P/P_o = 0.09$ at $x/L \approx 0.35$ up to the nozzle exit pressure.

To further highlight the differences between the cavitating nozzle flows of the three liquids, pressure measurement cases 3, 7, and 9 for $P_b = 20$ kPa are presented together in

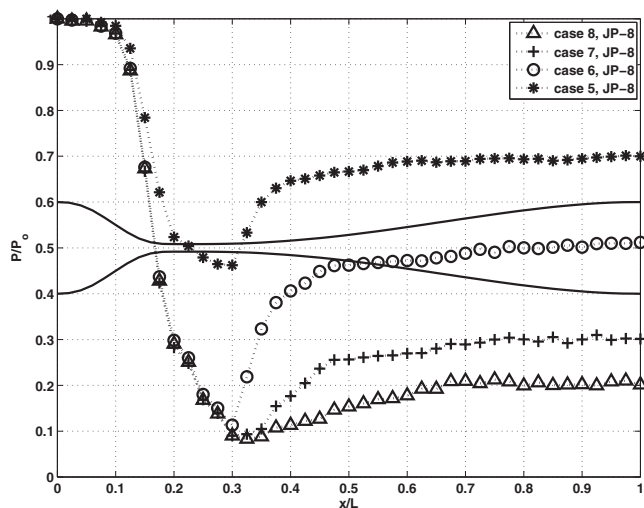


FIG. 10. Axial pressure distribution in JP-8, cases 5–8.

Fig. 11, including an expanded-view inset for the x/L range from 0.30 to 0.50. Differences in the character of the pressure recovery for the three cavitating flows are apparent. The discontinuous pressure increases associated with standing bubbly shocks were evident for water (from $x/L \approx 0.40$ to $x/L \approx 0.45$) and dodecane (from $x/L \approx 0.35$ to $x/L \approx 0.38$), as denoted by the solid lines in the inset. In contrast, the pressure recovery for JP-8 was extended spatially over the range from $x/L \approx 0.30$ and $x/L \approx 0.70$. The pressure increase for the dodecane was approximately 50% of that observed for water at the same back pressure. Recall that no shocklike bubble-collapse region appeared in the high-speed images of dodecane. Further, the pressure decreased more rapidly in the converging section of the nozzle for the JP-8 as compared to that for either water or dodecane. Void fraction measurements (presented later in this section) suggest that this was associated with an earlier onset of cavitation for the JP-8, which gave rise to a higher-velocity liquid phase and a lower static pressure.

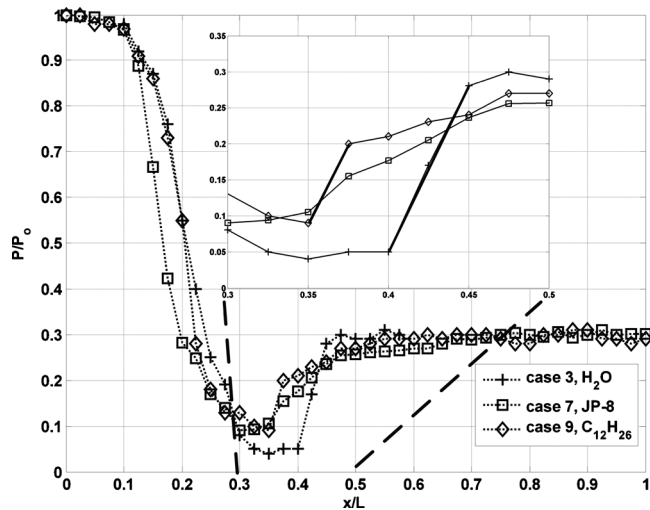


FIG. 11. Axial pressure distributions in H_2O , JP-8, and $C_{12}H_{26}$, cases 3, 7, and 9.

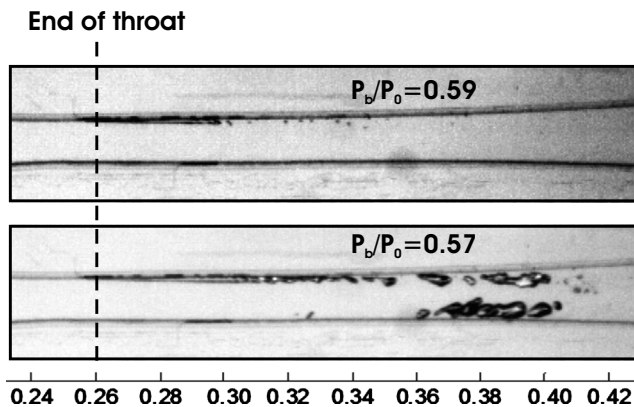


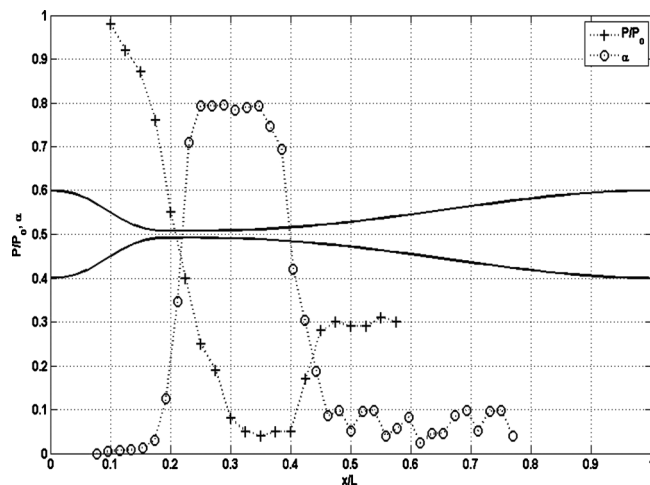
FIG. 12. Images of the onset of cavitation in H_2O at $P_b/P_0=0.59$ and $P_b/P_0=0.57$ (frame rate of 15 000 frames/s; exposure duration of $8 \mu s$) from $x/L=0.24$ to $x/L=0.42$.

4. Cavitation inception

It is well known that nucleation sites are necessary to catalyze the bubble growth that produces cavitation. Classical homogeneous or heterogeneous nucleation theory requires very high levels of supersaturation to create gas cavities and usually is associated with ultrapure liquids. This type of cavitation does not occur in most practical situations. More relevant to the current investigation is nucleation associated with some initial quantity of gas or vapor that serves to initiate the bubble growth process. Pre-existing gas and/or vapor-containing sites, which can be on the solid surfaces that confine the liquid or on microparticles within the liquid, can lead to the occurrence of nucleation events at or above the liquid vapor pressure. Concave surface cracks and pits will stabilize gas and vapor pockets, thereby serving nucleation sites.^{28–30} Although no nucleation studies have been performed in fuel, it would seem that the basic physics governing nucleation in fuel should be similar.

The onset of cavitation was manifested by microbubbles being formed and released either from corners of the nozzle’s throat or from corners immediately downstream of it. Only for subsidiary experiments in which the liquid was loaded highly with contaminant microparticles was cavitation inception observed to occur in the bulk of the liquid (see the bottom image in Fig. 3). Cavitation never was seen to initiate in the bulk of the fluid, even under magnified high-speed digital images. The onset occurred at an imposed back pressure ratio greater than that necessary to choke the flow, typically at $P_b/P_0=0.59$ for both water and JP-8. At an imposed back pressure ratio slightly above this value, the flow was single-phase liquid throughout the nozzle.

Figure 12 displays individual-frame visualizations of flow within the throat region for water at two different imposed back pressure ratios, $P_b/P_0=0.59$ and $P_b/P_0=0.57$. At $P_b/P_0=0.59$, microbubbles on the order of $50 \mu m$ in diameter formed at wall-corner sites, then proceeded to grow and collapse almost immediately downstream. The formation site was at $x/L \approx 0.25$, which was near the end of the throat. The microbubbles collapsed at $x/L \approx 0.31$, just beyond the throat. When the imposed back pressure ratio was lowered slightly to $P_b/P_0=0.57$, microbubbles still formed at approximately

FIG. 13. Axial void fraction distribution in H₂O, case 3.

the same location. However, the extent of cavitation increased noticeably, leading to microbubble collapse at $x/L \approx 0.40$. Results having the same trends were obtained for JP-8. As the imposed back pressure ratio was lowered further, the region of cavitation extended farther downstream and eventually filled the entire nozzle cross-section. This situation yielded fully choked conditions, as in the images of Fig. 6.

5. Void fraction measurements

The axial distribution of void fraction for water at a back pressure of $P_b = 20$ kPa is shown in Fig. 13 (case 3 in Table I). Pressure measurements also are included in the figure to illustrate the correlation between the pressure and void fraction.

As the static pressure decreased in the nozzle and bubbles were formed, the void fraction increased sharply from a value near zero at $x/L = 0.10$ to a maximum of $\alpha = 0.8$ at $x/L = 0.25$. The downstream bubble-collapse region location was highly localized, as the void fraction decreased rapidly between $x/L = 0.35$ and $x/L = 0.46$. Figure 13 shows the sudden decrease in void fraction occurred over the same range of x/L as did the pressure rise associated with the standing bubbly shock. Downstream of the bubble-collapse region, the void fraction varied between approximately 5% and 10% in a repeatable, almost spatially periodic fashion. This behavior was suggestive of the bubble rebound events that often characterize solutions of the Rayleigh–Plesset equation.⁸ The corresponding flow visualization image shows that this region contained a dilute mixture of spherical bubbles.

Corresponding void fraction measurements for the JP-8 case are presented in Fig. 14 (case 7 in Table I). The onset of cavitation for the JP-8 occurred farther upstream than for water. The void fraction for JP-8 suddenly increased to 10% by $x/L = 0.15$. In comparison, the void fraction for water was only 0.7% at $x/L = 0.15$ (see Fig. 13). The solubility of air in JP-8 is approximately 7.2 times the solubility of air in water at the same conditions. It is conjectured that a higher content of dissolved gas in JP-8 was responsible for the more rapid

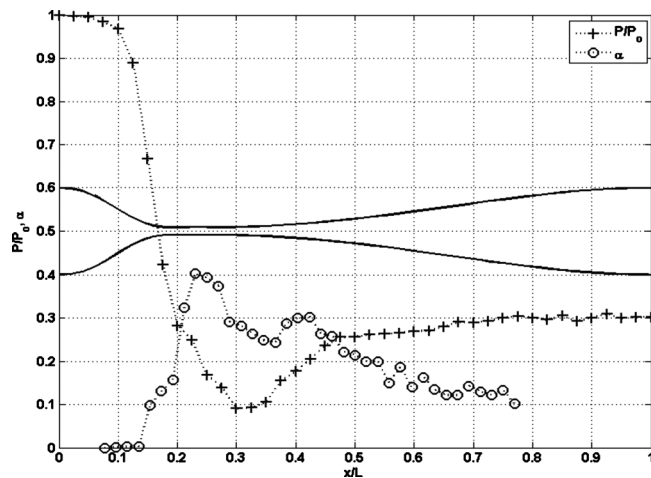
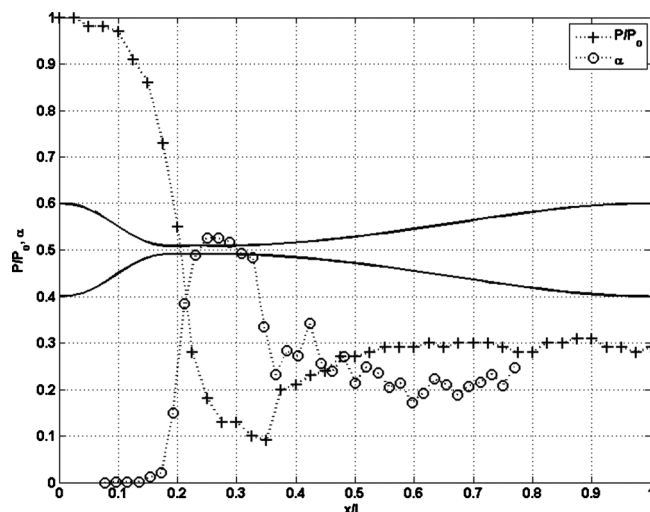


FIG. 14. Axial void fraction distribution in JP-8, case 7.

onset of gaseous cavitation in JP-8 than in water. Using the measured disparity in local void fraction between water and JP-8 at $x/L = 0.15$ and accounting for the density differences between the two liquids, the calculated static pressure difference between the two liquids was $\Delta P/P_0 = 0.21$. This agreed (within experimental uncertainty) with the measured pressure difference at $x/L = 0.15$, as shown in Fig. 11. This supports that the lower static pressure for JP-8 in the nozzle contraction was associated with earlier cavitation inception.

The void fraction for JP-8 increased to reach its maximum value of 40% at $x/L = 0.23$. Unlike the water case, there was no sudden bubble-collapse region for the JP-8. The JP-8 void fraction decreased gradually to reach a local minimum of approximately 25% at the $x/L = 0.37$ location. This was followed by another increase of approximately 5% up to the $x/L = 0.42$ location. This spatial variation in JP-8 void fraction was very repeatable over many trials. It is possible that this second increase in void fraction represented the spatially localized rebound growth of collapsing bubbles, as seen in the Rayleigh–Plesset model description of bubble dynamics. The slower decrease in void fraction in the nozzle's divergent section (as compared to water) marked the persistence of bubbles throughout the divergent portion of the nozzle.

Void fraction measurements for the corresponding dodecane case are shown in Fig. 15 (case 9 in Table I). The initial growth in void fraction occurred near $x/L = 0.15$, where the measured void fraction was approximately 1%. This value was lower than that for JP-8 at the same x/L location. Calculations showed the void fraction difference accounted for the lower static pressure in the nozzle contraction for JP-8 compared to dodecane, as shown previously in Fig. 11. The dodecane void fraction exhibited downstream growth, reaching a maximum value of approximately 53% at $x/L = 0.25$. A plateau of comparable void fraction values persisted to nearly $x/L = 0.30$, whereupon there was a rapid reduction in a single localized bubble-collapse region from $x/L = 0.30$ to $x/L = 0.36$. The void fraction was reduced by 23% over this interval. This reduction correlated very well with the pressure rise that occurred over the same region. The bubble collapse was followed by a 10% increase in void fraction from $x/L = 0.36$ to $x/L = 0.42$. Beyond $x/L = 0.42$, void frac-

FIG. 15. Axial void fraction distribution in $C_{12}H_{26}$, case 9.

tion decreased overall in response to the increasing static pressure but continued to undergo small amplitude spatial oscillations.

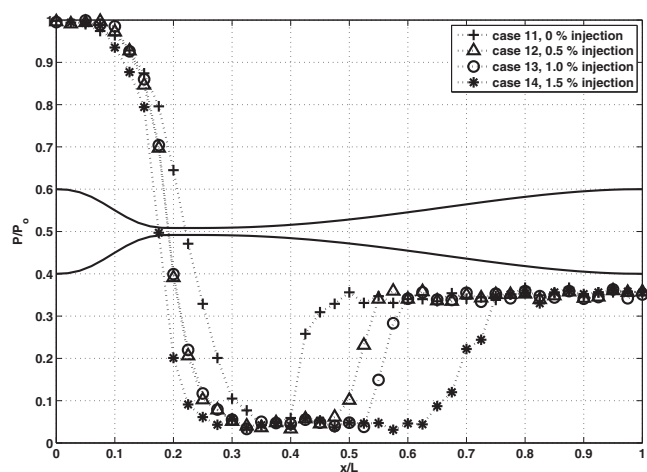
B. Experiments with microbubble injection

A series of experiments was performed in which microbubbles of air were injected into the C-D nozzle inlet through five hypodermic needles (Popper & Sons, Inc., No. 7102 hypodermic needle, 310 μm outer diameter and 160 μm internal diameter), located immediately upstream of the nozzle inlet. The initial diameter of the microbubbles was $\sim 160 \mu\text{m}$. The volumetric flow rate of the injected air was measured as described previously. The initial void fraction resulting from the injected air was determined from the measurement of the volumetric flow rates of the air and of the liquid. The mass flow rates were subsequently determined based on the measured static pressure at the inlet. The amount of gas that was injected was controlled by precision metering valves, such that the initial void fraction range was varied systematically from $\alpha_o = 0.5\%$ to $\alpha_o = 1.5\%$.

Table II summarizes the different operating conditions for the bubble injection experiments. For all eight cases presented in Table II, flow through the nozzle was choked. Additional experiments (*not* listed in this table, but to be discussed later) were conducted in water to identify the bubbly

TABLE II. Operating conditions for microbubble injection experiments.

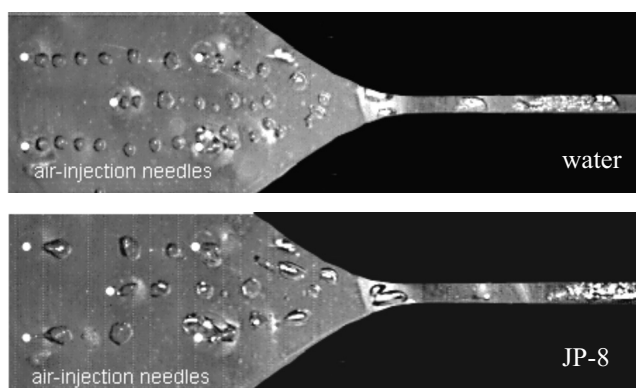
Case	Fluid	P_b (kPa)	α_o (%)	Q (L/min)
11	H ₂ O	20 \pm 1	Nascent	3.8 \pm 0.4
12	H ₂ O	20 \pm 1	0.50 \pm 0.06	3.8 \pm 0.4
13	H ₂ O	20 \pm 1	1.00 \pm 0.03	3.8 \pm 0.4
14	H ₂ O	20 \pm 1	1.50 \pm 0.02	3.8 \pm 0.4
15	JP-8	20 \pm 1	Nascent	4.2 \pm 0.4
16	JP-8	20 \pm 1	0.50 \pm 0.06	4.2 \pm 0.4
17	JP-8	20 \pm 1	1.00 \pm 0.03	4.2 \pm 0.4
18	JP-8	20 \pm 1	1.50 \pm 0.02	4.2 \pm 0.4

FIG. 16. Effect of initial void fraction on the axial pressure distribution in H₂O, cases 11–14.

shock location as a function of both P_b and α_o . For those experiments, the initial void fraction was varied from approximately 0.3% to 2.0% for three different back pressures (10 kPa, 15 kPa, and 20 kPa, corresponding to nozzle exit-to-inlet pressure ratios of approximately 0.10, 0.15, and 0.20), each producing fully cavitated flow.

The streamwise nozzle static pressure distributions for different initial void fractions were measured for the cases summarized in Table II. The results for water (cases 11–14) are shown in Fig. 16. Also shown at the top of Fig. 17 is a corresponding digital image of the water flow from the location of bubble injection to the nozzle throat for case 13. Figure 16 clearly shows the effect of initial void fraction on the streamwise location of the bubbly shock. As the initial void fraction increased, the location of the shock moved farther downstream toward the nozzle exit.

Beyond the nozzle throat there is a balance between bubble growth and wall divergence. Low local static pressure drives bubble growth and, in turn, gives rise to voids that occupy part of the flow cross-sectional area and, hence, produces high liquid velocity. To maintain this balance over a

FIG. 17. Images of H₂O (top) and JP-8 (bottom) cavitating mixtures with bubble injection, cases 13 and 17, respectively, showing flow within both the bubble injection region that is immediately upstream of the nozzle and the nozzle up to $x/L \approx 0.4$. Each of the five injection needle ends shown in each image is indicated by white dots.

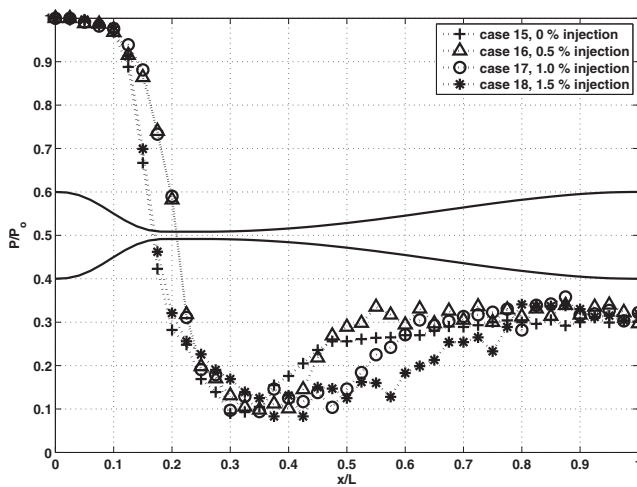


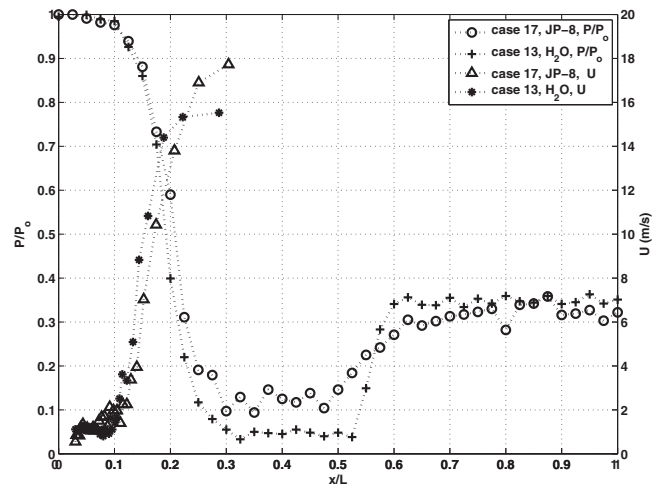
FIG. 18. Effect of needle injection in JP-8 cases 15–18.

given streamwise region requires sufficient initial void. Once the initial void is depleted, wall divergence dominates over bubble growth and sudden bubble collapse occurs. This is consistent with Fig. 16, which shows that the bubble-collapse location moves downstream as α_o increases. The initial void fraction also had a significant effect on the pressure in the nozzle contraction. At a given x/L location, the static pressure decreased as α_o increased. With increased local void fraction, the liquid flow cross-sectional area was effectively reduced, thereby requiring higher liquid phase velocity and lower static pressure.

The pressure distributions for JP-8 (cases 15–18 in Table II) are presented in Fig. 18 for different initial void fractions. A digital image of the flow for case 17 is shown at the bottom of Fig. 17. Pressure recovery in the diverging section was more abrupt than for the case with no air injection shown previously in Fig. 10. Bubble injection into the nozzle inlet had the effect of spatially organizing the structure of the bubble-collapse region. The location of this region in JP-8 was more evident, although the region was still less localized than in water. As the initial void fraction increased, the location of the bubble-collapse region moved farther downstream toward the nozzle exit, as was the case for water. For all bubble injection cases, cavitation inception occurred in the bulk of the fluid and not at the nozzle corners.

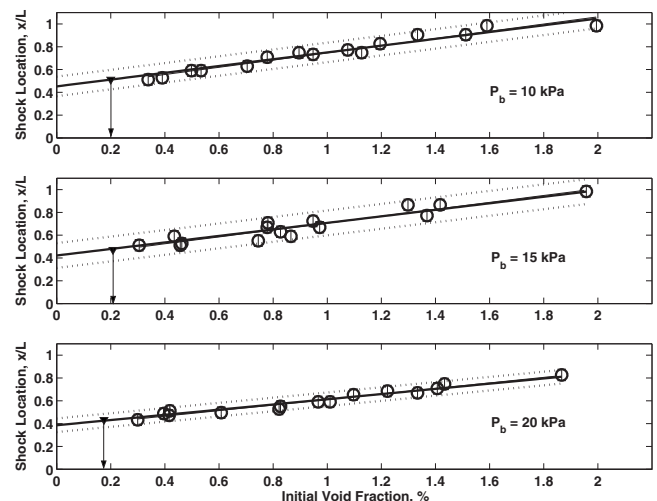
The pressure distributions for water and JP-8 with $\alpha_o=1\%$ (cases 13 and 17) are compared in Fig. 19. Also included in the figure is the velocity variation of the injected bubbles from the nozzle inlet to the throat. These velocity measurements were based on tracking individual bubbles in high-speed video images. This technique was employed until the bubbles underwent rapid growth and could not be tracked reliably.

The differences in the spatial localization of the bubble-collapse region are more evident in the pressure distributions shown in Fig. 19. While the bubble-collapse region for both water and JP-8 was centered at approximately $x/L=0.55$, the pressure increase for water occurred over a streamwise distance of approximately $\Delta x/L=0.05$, as compared to approximately $\Delta x/L=0.15$ for JP-8. The minimum

FIG. 19. Velocity and pressure distributions in JP-8 and H₂O for 1% gas injection, cases 13 and 17.

pressure achieved for water was lower than that for JP-8 ($P/P_o=0.05$ versus $P/P_o=0.12$). Even after taking into account the stated uncertainties in the volumetric flow rates for cases 13 and 17, the measured bubble speeds near the throat in Fig. 19 are well below the nominal throat speeds for JP-8 and water (28 m/s and 25.3 m/s, respectively). This strongly suggests that there is a significant velocity difference (slip) between the liquid and gas phases, which has important implications in model development.

The location of the bubble-collapse region for water was identified visually in another series of experiments, in which the initial void fraction immediately upstream of the nozzle inlet was varied systematically from approximately 0.3% to 2.0%. The axial location of the shock is displayed as a function of the initial void fraction in Fig. 20 for three different imposed back pressure conditions ($P_b=10$ kPa, $P_b=15$ kPa, and $P_b=20$ kPa). In each case, the shock location relative to the nozzle inlet increased from $x/L=0.4$ to $x/L=1.0$ (where bubble collapse was observed to occur beyond the nozzle exit) as the initial void fraction increased

FIG. 20. Location of bubble-collapse region as a function of initial void fraction in H₂O. The arrow identifies the nascent initial void fraction, $\alpha_{o,n}$.

from $\alpha_o=0$. (the so-called nascent case) to $\alpha_o \approx 2\%$. This trend was similar to that reported by Sandhu and Jameson¹⁹ for a different nozzle and type of two-phase mixture. However, the volume fractions examined in their study were approximately 10–50 times larger than in the present study.

Also shown in Fig. 20 are least-squares linear regression fits of the measurements for each back pressure case (indicated by solid lines) and their 95% confidence intervals (indicated by dotted lines). The experimental uncertainty in estimating the nondimensional shock location, x/L , was ± 0.05 (indicated by the relatively small error bars), or approximately 10%. This uncertainty resulted from spatial-temporal fluctuations in the position of the shock. Fluctuations of this nature also were reported by Muir and Eichorn¹⁸ and by Sandhu and Jameson,¹⁹ both being approximately 10%.

Most models of cavitating flow require an estimate of a nascent initial void fraction. The nascent initial void fraction, $\alpha_{o,n}$, corresponding to the measured shock location for the case when no bubbles were injected at the inlet, can be determined for each of the three back pressure cases using their respective best-fit lines. This method resulted in $\alpha_{o,n}$ values of 0.20%, 0.18%, and 0.21%, for the back pressures of 10 kPa, 15 kPa, and 20 kPa, respectively. These void fraction values are indicated by solid triangles with the downward-facing arrows in the figure. Because the three back pressure cases examined were all for cavitated flow, the values of $\alpha_{o,n}$ would be expected to be the same. Here, the void fraction values varied by at most 0.03%, with an average value of 0.19%. In essence, the value of $\alpha_{o,n}$ corresponds to the void fraction that is necessary to give a shock location as was measured for the nascent case. This technique could not be used for JP-8 and dodecane because specific shock locations could not be determined clearly in the high-speed images. As described in the following section, the nascent void fractions for the JP-8 and dodecane experiments can be inferred from the $\alpha_{o,n}$ for water and a single-fluid barotropic model.³⁶

IV. DISCUSSION AND CONCLUSIONS

The experiments reported herein clearly showed that the cavitation of JP-8 fuel exhibited noticeable differences from that of water for the same C-D nozzle geometry and nozzle pressure ratios. In this section, these differences are highlighted and plausible mechanisms for them are described.

In experiments with water in which the initial void fraction was controlled by air microbubble injection at the nozzle inlet, the average nascent void fraction in the absence of bubble injection was inferred to be $\alpha_o=0.19\%$. Using a single-fluid barotropic model,³⁶ the initial void fraction for either JP-8 or dodecane can be calculated from the measured choked flow mass flow rate and/or measured choked throat static pressures. This method gives $\alpha_{o,JP-8}/\alpha_{o,H_2O}=2.5$ and $\alpha_{o,C_{12}H_{26}}/\alpha_{o,H_2O}=3.6$, which implies initial nascent void fractions of $\alpha_o=0.5\%$ for JP-8 and $\alpha_o=0.72\%$ for dodecane. The higher nascent void fractions for JP-8 and dodecane are most likely associated with higher solubilities of air in those fluids than in water. For example, air is approximately seven times more soluble in JP-8 than in water at the temperatures the experiments were performed.

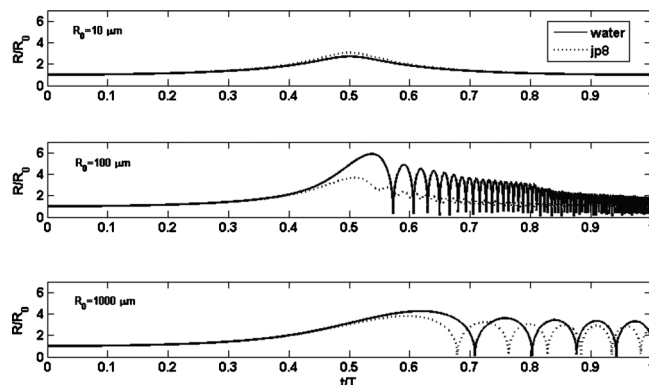


FIG. 21. Comparison of the dynamics of different-size bubbles for water and JP-8.

The fluid compressibility associated with streamwise bubble growth leads to fully choked nozzle flow for each fluid, as confirmed by direct mass flow rate measurements (see Fig. 4). Sonic throat conditions were also confirmed by using measured values of the local static pressure and the void fraction and a homogeneous bubbly flow model.¹⁹ For both water and JP-8, the sonic point at which the measured bubble velocity equaled the calculated mixture sonic velocity occurred within the throat of the nozzle. The sonic point for JP-8 was at $x/L=0.22$ and that for water was at $x/L=0.26$. Similar results were obtained using a barotropic model.³⁶

High-speed flow visualization showed that gaseous cavitation in water was characterized by the very rapid growth and subsequent merging of individual bubbles that gave rise to large slugs of vapor. In contrast, gaseous cavitation in both JP-8 and dodecane resulted in rather homogeneous mixtures of much smaller individual bubbles that showed no evidence of merging into larger voids. This observation was confirmed by void fraction measurements. Clearly, the mechanisms of bubble-bubble interaction differ between the fluids. For all three fluids, the presence of choked flow implies that the liquid and gas phases were well-mixed over the rectangular cross-section (no phase stratification).

The surface tension of the liquid must play an important role in the structure of the mixture, especially beyond a bubbly shock. The surface tension of water (7.2 mN) is more than three times that of JP-8 (2.3 mN) and of dodecane (2.5 mN). This has implications for both cavitation inception and bubble dynamics. Because the cosine of a bubble's surface contact angle is proportional to the liquid-gas surface tension, JP-8 and dodecane have better surface-wetting characteristics than water. This will lead to smaller nascent cavitation nuclei in JP-8 and dodecane as compared to water.

Fluid property differences also manifest themselves with regard to cavitation bubble dynamics. In order to qualitatively examine the roles that surface tension and viscosity play in nozzle cavitation, the solutions of the Rayleigh–Plesset equation for water and JP-8 are compared in Fig. 21. Nuclei radii spanning two orders of magnitude were considered: 10 μm , 100 μm , and 1000 μm . These covered the approximate range of bubble radii observed in the present experiments. A time-dependent cosine pressure distribution was assumed. This time-varying pressure was similar in es-

sential aspects to the pressure experienced by a bubble in traversing the C-D nozzle. T was 10 ms, which corresponded to the characteristic convective time scale of a fluid element inside the nozzle. For this distribution, the minimum pressure was $P/P_o=0.025$. Figure 21 shows that for very small nuclei, $O(10 \mu\text{m})$, both the water and JP-8 cases exhibited only weak growth. This size was of the order of the sizes of the nucleation sites measured on the nozzle-wall surface. In contrast, for intermediate size nuclei, $O(100 \mu\text{m})$, the water case exhibited rapid growth followed by classic bubble collapse and rebound events. In contrast, the JP-8 case exhibited more modest growth followed by a more gradual reduction in bubble size as the pressure increased. This size was of the order of the sizes of the bubbles and voids observed near the beginning of the shock region. JP-8 and water exhibited sudden bubble collapse only for very large nuclei, $O(1000 \mu\text{m})$. Although the results shown in Fig. 21 strictly are valid only for an isolated bubble, they are consistent with the results of the gaseous cavitation experiments presented in this study. In particular, Fig. 21 suggests that for the small bubbles observed in JP-8 and dodecane, the bubble collapse downstream of the throat will be more gradual than in water. This may explain, in part, the absence of a shocklike bubble collapse similar to that which occurred in water. Recall that evidence for the presence of a (comparatively weak) shock occurred in dodecane, but not in JP-8. Because JP-8 is a complex mixture of multiple hydrocarbons with widely disparate vapor pressures, it is also possible that this would have the effect of spatially extending the region of bubble collapse over a finite streamwise region and, thereby, prevent the formation of a localized shock.

Finally, it is noted that the experimental test section used in this investigation differs from components in aviation-fuel systems in terms of operating pressure, temperature, mass flow rate, flow geometry, and surface roughness. Yet, these experiments have characterized some of the basic aspects of fuel cavitation. These include nucleation and its subsequent bubble growth and collapse and choking. The primary differences between the three fluids examined can be explained by their different density, surface tension, viscosity, solubility of air, and the multiple components of JP-8 versus water and dodecane. The extensive measurements of static pressure void fraction profiles, bubble velocities, mass flow rates, and high-speed visualizations obtained in this study provide an accurate and thorough set of information. This should prove useful for the validation of models of fuel cavitation occurring in internal flows.

ACKNOWLEDGMENTS

The experimental results presented in this paper were part of the Ph.D. dissertation research of M. Davis and the M.S. thesis research of I. Dorofeeva. The authors acknowledge the role of M. Iqbal in the development of the experimental facility. This research was supported by the Honeywell Corporation. We especially thank Steve Emo, Corey Bourassa, and Abigail Parsons for their many technical interactions and support throughout this research.

- ¹B. L. Smith and T. J. Bruno, "Composition-explicit distillation curves of aviation fuel JP-8 and coal-based jet fuel," *Energy Fuels* **21**, 2853 (2007).
- ²H. T. Mayfield, "JP-8 composition and variability," Armstrong Laboratory, Environmental Research Division, Tyndall Air Force Base Report No. AL/EQ-TR-1996-0006, 1996, NTIS Order Number AD-A317 177/4.
- ³Coordinating Research Council, *Handbook of Aviation Fuel Properties*, 3rd ed. (Coordinating Research Council, Inc., Alpharetta, GA, 2004).
- ⁴T. Edwards and L. Q. Maurice, "Surrogate mixtures to represent complex aviation and fuel rockets," *J. Propul. Power* **17**, 461 (2001).
- ⁵S. Violi and E. G. Yan, "Experimental formulation and kinetic model for JP-8 surrogate mixtures," *Combust. Sci. Technol.* **174**, 399 (2002).
- ⁶R. T. Knapp, J. W. Daily, and F. G. Hammit, *Cavitation* (Institute of Hydraulic Research, University of Iowa, Iowa City, 1970).
- ⁷F. R. Young, *Cavitation* (Imperial College Press, London, 1999).
- ⁸C. E. Brennen, *Cavitation and Bubble Dynamics* (Oxford University Press, New York, 1995).
- ⁹C. E. Brennen, *Fundamentals of Multiphase Flow* (Cambridge University Press, New York, 2005).
- ¹⁰M. S. Plesset and A. Prosperetti, "Bubble dynamics and cavitation," *Annu. Rev. Fluid Mech.* **9**, 145 (1977).
- ¹¹R. E. A. Arndt, "Cavitation in fluid machinery and hydraulic structures," *Annu. Rev. Fluid Mech.* **13**, 273 (1981).
- ¹²R. E. A. Arndt, "Cavitation in vortical flows," *Annu. Rev. Fluid Mech.* **34**, 143 (2002).
- ¹³J. R. Blake and D. C. Gibson, "Cavitation bubble near boundaries," *Annu. Rev. Fluid Mech.* **19**, 99 (1987).
- ¹⁴D. Dowson and C. M. Taylor, "Cavitation in bearings," *Annu. Rev. Fluid Mech.* **11**, 35 (1979).
- ¹⁵E. Giannadakis, D. Papoulias, M. Gavaises, C. Arcoumanis, C. Soteriou, and W. Tang, "Evaluation of the predictive capability of diesel nozzle cavitation models," SAE Technical Paper Series No. 2007-01-0245, 2007, DOI: 10.4271/2007-01-0245.
- ¹⁶D. P. Schmidt, C. J. Rutland, and M. L. Corradini, "A numerical study of cavitating flow through various nozzle shapes," *SAE J. Engines* **106**, 1644 (1997).
- ¹⁷R. F. Tangren, C. H. Dodge, and H. S. Seifert, "Compressibility effects in two-phase flow," *J. Appl. Phys.* **20**, 637 (1949).
- ¹⁸J. F. Muir and R. Eichhorn, "Compressible flow of an air-water mixture through a vertical, two-dimensional nozzle," *Proceedings of the 1963 Heat Transfer and Fluid Mechanics Institute* (Stanford University Press, Stanford, CA, 1963), pp. 183–204.
- ¹⁹N. Sandhu and G. J. Jameson, "An experimental study of choked foam flows in a convergent-divergent nozzle," *J. Multiphase Flow* **5**, 39 (1979).
- ²⁰N. T. Thang and M. R. Davis, "Pressure distribution in bubbly flow through venturis," *Int. J. Multiphase Flow* **7**, 191 (1981).
- ²¹R. Ishii, Y. Umeda, S. Murata, and N. Shishido, "Bubbly flows through a converging-diverging nozzle," *Phys. Fluids A* **5**, 1630 (1993).
- ²²Y.-C. Wang and C. E. Brennen, "One-dimensional bubbly cavitating flows through a converging-diverging nozzle," *ASME J. Fluids Eng.* **120**, 166 (1998).
- ²³A. Crespo, J. García, and J. Jiménez-Fernández, "Stability criteria of the steady flow of a liquid containing bubble along a nozzle," *ASME J. Fluids Eng.* **123**, 836 (2001).
- ²⁴A. T. Preston, T. Colonius, and C. E. Brennen, "A numerical investigation of unsteady bubbly cavitating nozzle flows," *Phys. Fluids* **14**, 300 (2002).
- ²⁵C. F. Delale, G. H. Schnerr, and J. Sauer, "Quasi-one-dimensional steady-state cavitating nozzle flows," *J. Fluid Mech.* **427**, 167 (2001).
- ²⁶C. F. Delale, K. Okita, and Y. Matsumoto, "Steady-state cavitation nozzle flows with nucleation," *ASME J. Fluids Eng.* **127**, 770 (2005).
- ²⁷"JP-8 Volatility Study," Southwest Research Institute Report No. IERA-RS-BR-SR-2001-0002, 2001, NTIS Order Number ADA394279.
- ²⁸R. E. Apfel, "The role of impurities in cavitation—Threshold determination," *J. Acoust. Soc. Am.* **48**, 1179 (1970).
- ²⁹M. Strasberg, "Onset of ultrasonic cavitation in tap water," *J. Acoust. Soc. Am.* **31**, 163 (1959).
- ³⁰K. A. Mørch, "Cavitation nuclei and bubble formation—A dynamic liquid-solid interface problem," *ASME J. Fluids Eng.* **122**, 494 (2000).
- ³¹G. Liger-Belair, M. Vignes-Adler, and C. Voisin, "Kinetics of gas discharging in a glass of champagne: The role of nucleation sites," *Langmuir* **18**, 1294 (2002).
- ³²D. Mackay, W. Y. Shiu, and K. C. Ma, *Illustrated Handbook of Physical-Chemical Properties and Environmental Fate for Organic Chemicals* (Lewis, Ann Arbor, MI, 1993), Vol. III.
- ³³F. M. White, *Fluid Mechanics*, 6th ed. (McGraw-Hill, Boston, MA, 2006).

- ³⁴A. Ulas, "Passive flow control in liquid-propellant rocket engines with a cavitating venturi," *Flow Meas. Instrum.* **17**, 93 (2006).
- ³⁵M. P. Davis, "Experimental investigation of the cavitation of aviation fuel in a converging-diverging nozzle," Ph.D. dissertation, University of Notre Dame, 2008.

- ³⁶See supplementary material at <http://dx.doi.org/10.1063/1.3490051> for "Cavitation of JP-8 Fuel in a Converging-Diverging Nozzle: Experiments and Modelling," by I. Dorofeeva, F. Thomas, and P. Dunn, presented at the 7th International Symposium on Cavitation, Ann Arbor, MI (2009).